RSC Advances

PAPER

View Article Online
View Journal | View Issue

Cite this: *RSC Adv.*, 2022, **12**, 29385

Adsorption of Mn(II) ions from wastewater using an AgNPs/GO/chitosan nanocomposite material†

Abeer El Shahawy, *[a] Mahmoud F. Mubarak,[bc] Merna El Shafie[a] and Hesham M. Abdulla[d]

Water contaminated with heavy metal ions is extremely poisonous and threatens living organisms. Therefore, scientists place a premium on removing heavy metal ions from water that has already been contaminated. Removing metal ions from water typically involves the use of nanomaterials. Chitosan was made by extracting it from shrimp shells and combining it with a 3 : 1 ratio of synthetically produced AgNPs/GO. Fourier transform infrared spectroscopy (FTIR), scanning electron microscopy (SEM) with transmission electron microscopy (TEM), and X-ray diffraction were used to investigate an AgNPs/GO/chitosan nanocomposite (XRD). A number of studies must be run to determine the optimal pH, adsorbent quantity, retention period, stirring speed, temperature, and initial concentration. The studies were conducted in a variety of ways. The isotherms of Langmuir, Freundlich, and Dubinin–Radushkevich were utilized. The industrial wastewater was used in the column adsorption experiment, and the flow rates and column bed heights were varied. An optimum contact time, pH, and adsorbent dosage for Mn(II) were determined. At 30 minutes, pH 6, and 0.05 grams of Mn(II) adsorbent per 100 ml, with agitation at 250 rpm, room temperature of 30 °C, and an initial concentration of 40 ppm, the best conditions were discovered. A positive correlation coefficient finding ($R^2 = 0.925$) indicates a good fit for Mn, according to equilibrium studies (II). The pseudo-second-order active model was connected to data that suited the pseudo-first and pseudo-second-order models. In the intra-particle diffusion model, the mechanism must proceed through four phases before equilibrium is reached. In an industrial adsorbent column, the adsorbent was put to the test. The periodicity test demonstrates that the nanocomposite's adsorption capability can be recovered by washing it with 0.1 M HCl. Mn(II) adsorbed on AgNPs/GO/Chitosan after four cycles was only 20%, insufficient for additional adsorption tests. The repeated cycles that led to the partial loss of the adsorbate may have reduced the adsorbent material's efficacy.

Received 27th July 2022
Accepted 4th October 2022

DOI: 10.1039/d2ra04693h

rsc.li/rsc-advances

1. Introduction

Indeed, water is one of the most fundamental elements of life. We can't have plants or animals without water. There can be no life on earth if there is no water. As we go into the third millennium, the availability of clean drinking water has emerged as a pressing global issue. Excessive levels of heavy metals in the environment can have detrimental effects on human health and ecosystems.[1,2] A powerful physicochemical method is an adsorption to separate and filter water and wastewater. Due to its low operating costs, high treatment effectiveness without discharging any toxic by-products, straightforward recovery, and reusable adsorbent, adsorption has emerged as the most widely used treatment procedure for removing heavy metals from aqueous solutions.[3] Adsorption is now a good removal method for developing regions due to its ease of operation, regeneration capability, and low toxic sludge creation. Natural, locally available adsorbent-based processes are regarded as more accessible for developing nations, have a lower investment cost, and have a smaller environmental impact (CO_2 emission).[4] Adsorption may remove impurities from both types of water. It is the method of choice for removing dangerous heavy metals, retrieving and recycling them. Treatment of industrial wastewater containing metals is quite intriguing.[5] Heavy metals are harmful to humans, animals, and plants, even at very low concentrations, which is the fundamental reason for this. One of the most pressing problems facing the globe today is environmental pollution. Chemical pesticides and fungicides used for both agricultural and non-agricultural uses have left residues in the water, air, plants, and soil that are damaging to the environment and people.

[a]*Department of Civil Engineering, Faculty of Engineering, Suez Canal University, PO Box 41522, Ismailia, Egypt. E-mail: abeer_shahawi@eng.suez.edu.eg; mernaelshafie24@gmail.com*

[b]*Petroleum Applications Department, Egyptian Petroleum Research Institute (EPRI), Nasr City 11727, Cairo, Egypt. E-mail: fathy8753@epri.sci.eg*

[c]*Faculty of Science, Mansoura University, Mansoura, Egypt*

[d]*Botany Dept., Faculty of Science, Suez Canal University, Box 41522, Ismailia, Egypt. E-mail: hesham_abdulla@science.suez.edu.eg*

† Electronic supplementary information (ESI) available. See DOI: https://doi.org/10.1039/d2ra04693h

Additionally, they bioaccumulated throughout the food chain.[6] In agriculture, fungicides and some of their metabolic products are used to manage various fungal infections in various crops (vegetables, fruits, medicinal plants, and ornamentals).[7] Recent years have seen a rise in interest in nanotechnology. Nanomaterials stand out from bulk materials thanks to their large surface areas, chemical stability, and resilience to environmental influences. Low surface area densities eventually lead to big stable nanoparticles since adsorption energy and stability of nanoparticle size are correlated.[8–13] These nanomaterials can effectively remove them from their environmental sources by adsorbing fungicides and heavy metal ions on their surface. Nanoparticles have the potential to facilitate the efficient removal of metals as well as organic and inorganic pollutants from water.[14–21] Nano-hydroxyapatite is a suitable material for the disposal of contaminants due to its strong adsorption ability for heavy metals, according to ref. 6,22–24. An alternate adsorbent to remove heavy metals and pesticides is nano-bentonite; bentonite is widely available and reasonably priced. Montmorillonite minerals are the primary components of nano-bentonite. Due to the three layers in montmorillonite, negative charges develop on the surface. Heavy metals can be removed using this component, which has an active site.[7] For Cd and Hg, nano-bentonite adsorbs heavy metals with a 99.03 and 99.18 percent efficiency, respectively.[8,25] It presents wonderfully. Nanotechnology is the most effective approach for eliminating heavy metals from wastewater.[26,27] Nanomaterials are higher-performing technology. Nanomaterials are suitable for water treatment applications due to their high surface-to-volume ratio, high surface energy, and improved catalytic activity. The absorbent substance used in this experiment has various potential commercial applications in the future. In this study, the most common new waste biomass, AgNPs/GO/Chitosan nanocomposite, would be used to demonstrate how Mn(II) would adsorb on these nanocomposite materials. The findings indicate that AgNP/GO/Chitosan absorbent material is economically appealing for wastewater treatment. GO is an excellent candidate for support materials that improve AgNP dispersion and materials with enhanced mechanical strength. Furthermore, GO would benefit the economy because of its low production costs and ease of use. The composite form will combine the benefits of AgNPs and GO, particularly the charges on the GO surface that absorb reactants *via* a – stacking interaction, resulting in a larger concentration of agents near the AgNPs on the surface and hence more efficient contact between reactants.[28]

In addition, the proportion of silver used in nanocomposite is much lower than that of other components, which are less expensive than silver, making it cost-effective. AgNP/GO/Chitosan absorbent material has demonstrated excellent adsorption performance with high and low manganese levels, simple pretreatment of the absorbent material, and high desorption and sorption capacity regeneration feasibility. Due to the chitosan derived from shrimp shellfish, nano silver protects the nanocomposite against bacterial buildup and enhances the lifetime of the nanocomposite. These characteristics will contribute to the material's future use as an absorbent for removing heavy metals from industrial wastewater.[29] The main objective of this study was to ascertain the viability of AgNPs/GO/Chitosan Nanocomposite as a low-cost biosorbent for Mn(II) adsorption from wastewater. The batch adsorption procedure was examined at room temperature by the following operational parameters: initial pollutant concentration, contact time, adsorbing dose, and stirring rate. XRD, Fourier transform infrared spectroscopy, scanning electron microscopy, and transmission electron microscopy were employed to investigate the adsorbing substance under various circumstances. The kinetic models, diffusion equations, and empirical isotherms were all applied.

2. Materials & methods

2.1. Prepared adsorbent

2.1.1. Chitosan & AgNPs/GO/chitosan synthesis. The composite was prepared and synthesized according to El Shahawy *et al.* (2022)[30] (see Fig.1). The companies for the purchased and used materials are displayed in Table 1.

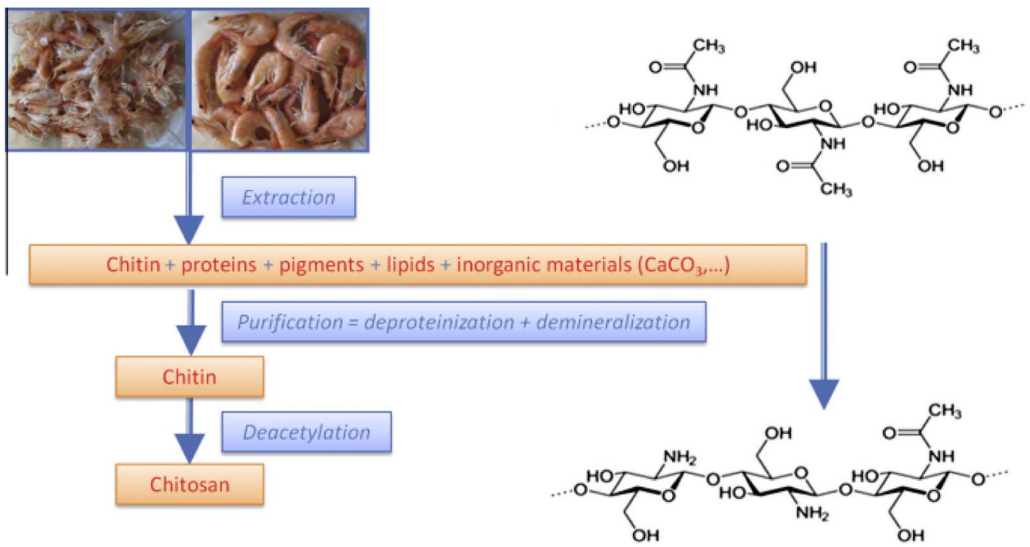

Fig. 1 Process for the production of chitosan from crustacean shell waste.

Table 1 The companies for the used materials

No.	Materials	Company
1	Industrial wastewater	Rocket fertilizer factory in new Salhia, Sharqia, Egypt
2	Chitosan	Local market, Ismailia, Egypt
3	Hydrochloric acid	Alpha chemika, Egypt
4	Sodium hydroxide	Alpha chemika, Egypt
5	Graphite powder	Alpha chemika, Egypt
6	Silver nitrate	Alpha chemika, Egypt
7	Sodium borohydride	Oxford lab fine chem LLP, Egypt
8	Trisodium citrate dihydrate	Oxford lab fine chem LLP, Egypt
11	Manganese chloride	Oxford lab fine chem LLP, Egypt

2.2. Adsorption parameter optimization

The study considered six factors (pH, contact time, adsorbent dose, temperature, agitation speed, and manganese content) to assess the nanocomposite material to adsorb (Mn) (Table 2).

2.3. Testing protocols

2.3.1. Adsorbent examination. At 196 °C, the adsorbent texture was examined. Samples were heated for two hours at 150 °C under a vacuum to remove surface gas (10^{-4} Torr). The

Table 2 The experimental program

Test 1		Test 2		Test 3		Test 4		Test 5		Test 6	
time	60	time	variable	time	30	time	30	time	30	time	30
PH	variable	PH	6	PH	6	PH	6	PH	6	PH	6
temp	30	temperature	30	temperature	30	temperature	variable	temperature	30	temperature	30
Co	40	conc	40	conc	40	conc	40	conc	50	conc	variable
stirrer	9	str	9	str	9	str	9	str	variable	str	9
dosage	0.02	dosage	0.02	dosage	variable	dosage	0.02	dosage	0.02	dosage	0.02

2.2.1. Batch experiments of manganese Mn(II). 7.92 g of manganese chloride, $MnCl_2$, was carefully dissolved in 100 ml of distilled water to provide a stock solution of Mn(II) (1000 ppm). The standard solution was diluted with distilled water to create the Mn(II) standard solution. 0.05 g of AgNP/GO/Chitosan and 100 ml of a 50 ppm Mn(II) solution were used in the equilibrium procedure. At a speed of 250 (rpm), samples were shaken for 30 minutes. Using a spectrophotometer, the centrifuged samples were examined for Mn(II) ions. 0.1 M HCl and 0.1 M NaOH were used to change the pH. This study examined pH (from 2 to 8), contact time (10 to 80 min), adsorbent dose (0.01 to 0.5 g), temperature (30 °C to 80 °C), agitation speed (100 to 250 rpm), and concentration of Mn(II) (5 to 400 ppm) on the adsorbent's ability to remove Mn(II) as shown in Table 2.

The pollutant removal and adsorption capacities at equilibrium were determined using the following equations:

$$\% \text{ removal} = (C_o - C_e)/C_o \times 100 \quad (1)$$

$$q_e = (C_o - C_e) \times V/W \quad (2)$$

As C_o and C_e, the initial Mn(II) and equilibrium concentrations are displayed (ppm). The solid's equilibrium adsorption capacity is q_e, measured in mg g^{-1}. W (g) is the weight of the dry adsorbent employed in the experiment, and V (ml) is the volume of the Mn-containing solution (II).

S_{BET} surface area was estimated using the BET equation for the adsorption isotherm branch as described by El Shahawy *et al.* (2022).[30]

2.3.2. Industrial wastewater sampling. A sample of the industrial effluent was provided by the rocket fertilizer plant in New Salhia, Sharqia, Egypt. Table 3 lists the most crucial properties of industrial wastewater. All the analyses were carried out according to standard water examination methods. Using a gravimetric method, the TDS of the filtrate was calculated. Mn was determined using conventional water testing procedures (II). The pH of the test water's raw water was adjusted using either 0.1 M NaOH or HCl (0.1 M). We exclusively utilize top-notch chemicals that come from the local market in Egypt (Table 1).

Table 3 The characteristics of the industrial's wastewater

Colour	pH	TSS (ppm)	COD (ppm)	TDS (ppm)	Mn (ppm)	Alk
Light grey	3.22	542	5500	9160	49.29	

2.3.3. Water analysis. Readings of pH were taken using the pH meter (AD1000). Atomic absorption methods have been used to analyze Mn(II) ions concentrations in raw and treated

water. (AAS), which makes use of the flammatic absorption spectrometer ZEEnitu 700P-Analytik Jena, Germany.

3. Results & discussion

3.1. Composite characterization

3.1.1. FTIR spectroscopy. With FTIR, the functional groups in the composite material that are in charge of Manganese Mn(II) sorption can be located. As depicted in Fig. 2, the infrared spectra of extract, GO, AgNP, Chitosan, and composites of AgNP GO and Chitosan were gathered. Maximum intensities and primary absorption peak sites in the FTIR spectra are between 500 and 4000 cm^{-1}. The bending vibrations of phenols, polysaccharides, and O–H in the GO are responsible for the AgNP/GO/Chitosan composites' 900 cm^{-1} absorption peak. The absorption peak at 800 cm^{-1} provides additional evidence of the C=O bond's existence. In this instance, a peak at 1600 cm^{-1} represents the C–O–H bond. A comparable signal at 3500 cm^{-1} was detected for the CH bond. Ag/GO nanocomposite is created *via* interactions between negatively charged GO ions and Ag^{+} cations because of the functional groups in GO (hydroxyl, epoxide, carbonyl, and carboxylic groups).

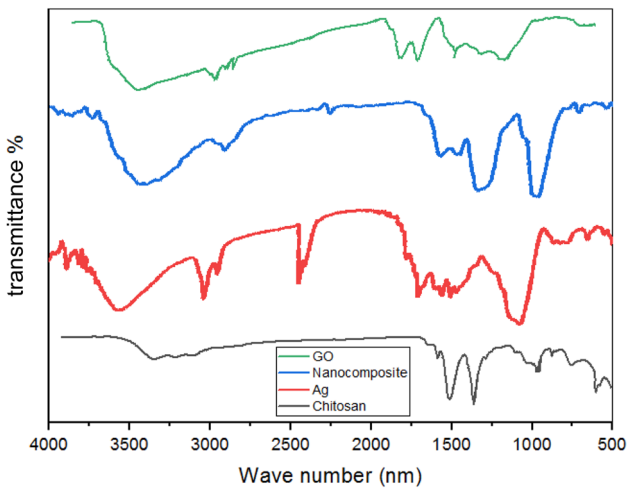

Fig. 2 FTIR of composites.

3.1.2. Scanning electron microscopy (SEM). AgNPs/GO/chitosan composite's surface morphology was identified by SEM, as shown in Fig. 3; SEM from the external surface of chitosan nanoparticles allowed analyzing the structural situation. SEM characterizes the surface morphology and average particle size of chitosan, chitin, and AgNPs/GO/chitosan composites. The surface morphology of chitin was coated with both bores and nanofibers, as illustrated in Fig. 3. The nanoparticles have an average particle size between 33.64 and 74.87 nm. Fig. 3(B) shows the microfibril chitin fibers' diameter, which ranges from 1–2 μm. SEM pictures demonstrated the continuous nature of the thin, multilayer membrane created by GO and the absence of macropores or other flaws. 150 nm is about how thick it is thought to be. Sheets of graphite oxide could be seen on their

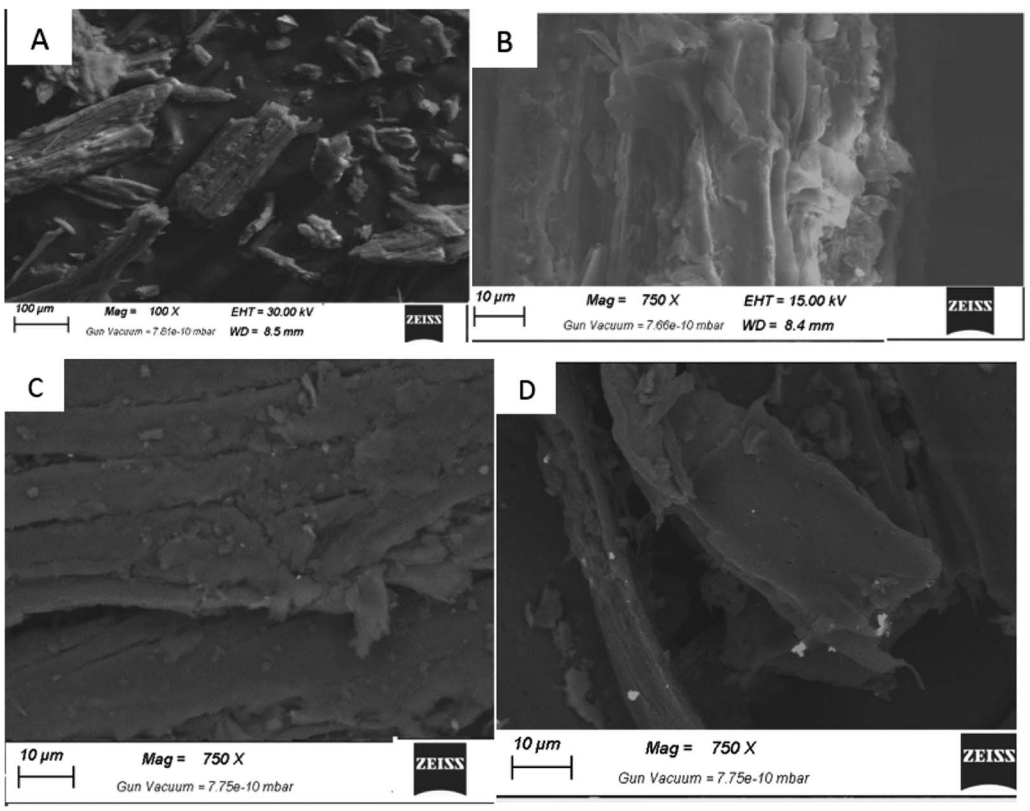

Fig. 3 SEM: (A) chitin, (B) chitosan, (C) AgNPs/Go/chitosan composite, and (D) Go.

surface. The AgNPs on the surface of the graphite oxide was discovered to be evenly distributed and interwoven, as shown in Fig. 3. The surface of activated graphite oxide is depicted in Fig. 3(D). The AgNPs/GO/chitosan composite morphology, as illustrated in Fig. 3, has a limited number of tiny longitudinal indentations and a great number of big bulges.

3.1.3. Transmission electron microscopy (TEM). AgNPs particles are anchored on GO, as shown in Fig. 4, according to the morphology of the nanocomposite of AgNPs and GO. Amorphous graphite oxide and AgNPs crystal characteristics could be identified. The AgNPs nanocrystals' tetragonal form is depicted in Fig. 4. All AgNPs/GO composites had particle sizes between 20 and 35 nm due to the same AgNPs preparation procedures. Regarding particle size, the TEM and XRD data showed a high agreement.

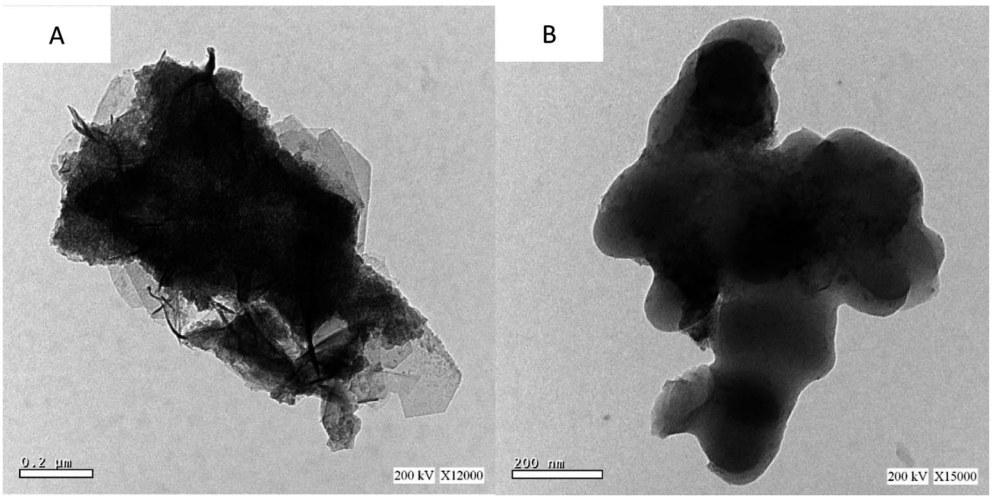

Fig. 4 TEM of (A) nanocomposite AgNPs/GO and (B) Go.

3.1.4. Surface charge analysis. AgNPs/GO/chitosan composite zeta potential measurements at a pH range of 2–8 are shown in Fig. 5. The AgNPs/GO/chitosan composite's zeta potential dropped as the pH was raised. The calculated point of zero charge (PZC) of AgNPs/GO/chitosan composite was 3. Thus, below these values, the adsorption of anionic ions is encouraged due to the positively charged surface of the adsorbent. The positive metal ion interacts electrostatically with the negative surface of the adsorbent (caused by the carboxyl/amine groups present) above the pHPCZs that have been seen. Thus, cationic adsorption is encouraged. In this experiment, the electrostatic attraction was exploited to adsorb metal ions.

3.2. Effect of pH

Fig. 6 depicts the effect of pH on Mn(II) varied from 2 to 10 at adsorbent dose = 0.05 g per 100 ml, Mn C_o = 40 ppm, contact time = 80 min, 30 °C, and agitation speed = 250 rpm. From 6.00 to 2.00, it is observed that adsorption capacity (q_e) and removal ratio (RR%) of manganese Mn(II) don't affect by alkaline or acidic media, the optimum removal ratio % RR reached 97.8% (r 0.849, p 0.069) and adsorption capacity (q_e) reached 78.24 mg g^{-1} (r 0.849, p 0.069) at pH 6, as shown in Fig. 6. This could be because for Mn(II) when the pH of the medium increases, the rivalry between positively charged metal ions and H^+ ions

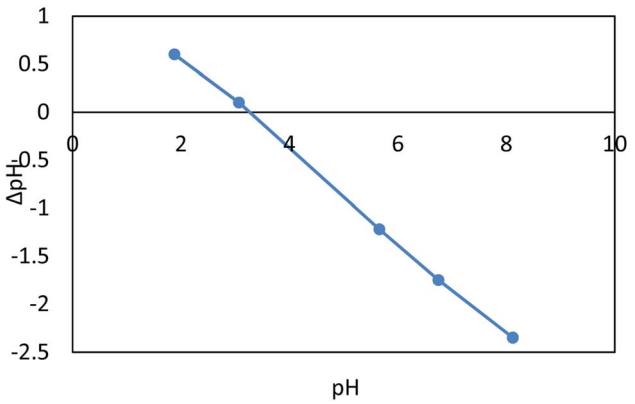

Fig. 5 The zeta (ξ) potential of AgNPs/Go/chitosan nanocomposite is a function of the solution's pH with no background electrolyte inclusion.

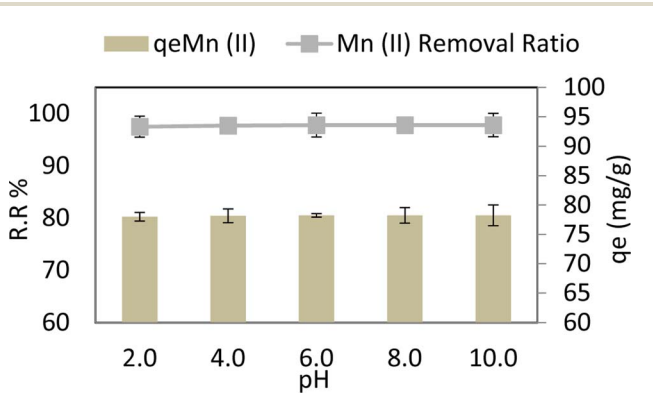

Fig. 6 pH effect on the adsorption removal efficiency and the capacity of Mn(II).

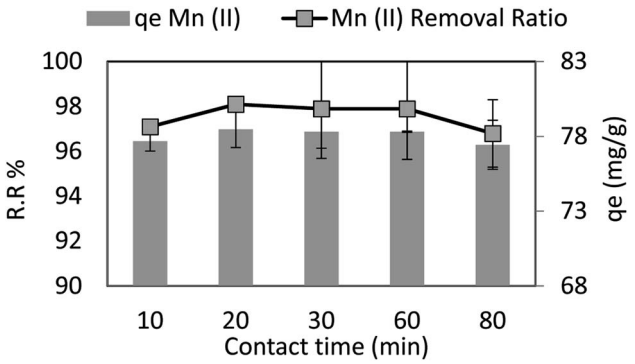

Fig. 7 The contact time effect on the removal efficiency and the adsorption capacity of Mn(II).

lessens. Metal ions become the predominant species to sorb on the AgNPs/GO/chitosan.[31] This is accurate in so far as positively charged species of the metal ions are present in the solution; this explains the elimination of Mn(II) ions in alkaline environments.

3.3. The effect of contact time

The test program carried out at contact time varied from 10 min to 80 min and in case of a dose = 0.05 g per 100 ml, pH = 6, Mn conc. = 40 ppm, and agitation speed = 250 rpm at 30 °C. It is observed that in the first 10 minutes of the test, adsorption capacity (q_e) and removal ratio (RR) of manganese (Mn) reached 77.68 mg g^{-1} and 97.1% R^2 (r 0.92, p 0.553), respectively, and they had no change by the time. This conclusion is consistent with other researchers' reported findings. Due to the large number of unoccupied surface patches in the initial stage that may be absorbed, as illustrated in Fig. 7, adsorbing species absorb quickly in the early contact time phases before slowing down toward equilibrium.

3.4. The effect of adsorbent dosage

Adsorbent dosage was changed from 0.01 to 0.5 g per 100 ml during the test program, which also included the following parameters: pH = 6, Mn conc. = 40 ppm, contact period of 30 min, and agitation speed of 250 rpm at 30 °C. It is noted that the adsorption capacity (q_e) and removal ratio (RR%) of manganese (Mn) increases as adsorbent dosage increases and is nearly kept slightly constant from 0.05 g to 0.5 g, as shown in Fig. 8. 0.05 g per 100 ml manganese solution is the most economic value of adsorbent dosage and the corresponding removal ratio % RR and adsorption capacity (q_e) for 0.05 adsorbent dosage were 97.8% (r 0.998, p 0.086) and 78.24 mg g^{-1} R^2 (r 0.595, p 0.120) respectively.

The metal-binding site ratio affects the adsorption capability. The availability of heavy metal ions was inadequate to completely saturate the open spots on the adsorbent surface at a higher dose. The increased accessible surface area and the active adsorption sites for Mn led to reduced ions absorption per unit mass of the adsorbent, resulting in lower adsorption capacity. There was no discernible increase, and a steady state of adsorption was seen for manganese when the adsorbent dose was raised from 0.05 to 0.5 gL^{-1}. For Mn(II), the adsorbent dose becomes negligible after the adsorption equilibrium is attained by increasing the adsorbent to more than 0.05. Nevertheless, as adsorbent concentrations rise, the diffusion falls due to a number of factors, such as a reduced solvent to adsorbent ratio, interference between binding sites, and electrostatic interactions.[32]

3.5. The effect of temperature

At an adsorbent dose of 0.05 g per 100 ml, a pH of 6, a Mn concentration of 40 ppm, a contact period of 30 min, and an agitation speed of 250 rpm, the temperature varied from 30 °C to 80 °C. Manganese (Mn) is shown to have a decreasing adsorption capacity (q_e) and removal ratio (RR percent) as the temperature rises. So maximum removal ratio % RR and adsorption capacity (q_e) reached 97.8% R^2 (r 0.99, p 0.01) and 78.24 mg g^{-1} R^{-2} (r 0.99, p 0.01) respectively at 30 °C as shown in Fig. 9. According to the findings, graphene oxide and chitosan contribute to chemical adsorption and physical adsorption caused by the pores and fissures in graphene oxide and the electron focus of silver ions that have been transformed into nanomaterial. Even so, as seen in Fig. 9, physical adsorption

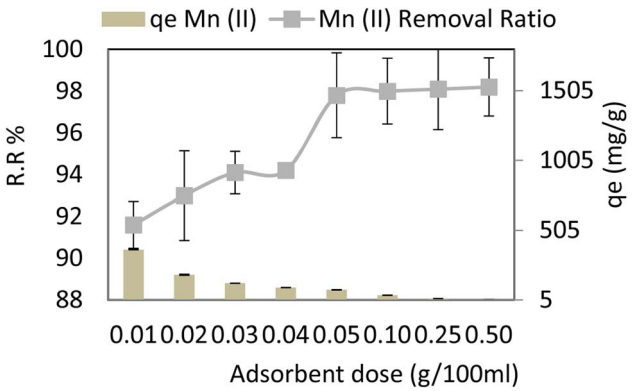

Fig. 8 The adsorbent dose effect on the removal efficiency and the adsorption capacity of Mn(II).

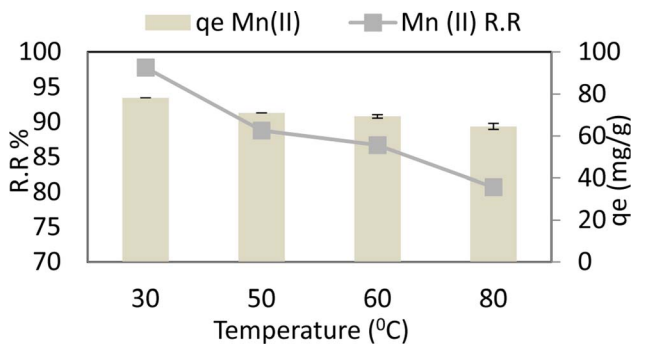

Fig. 9 The temperature effect on the removal efficiency and the adsorption capacity of Mn(II).

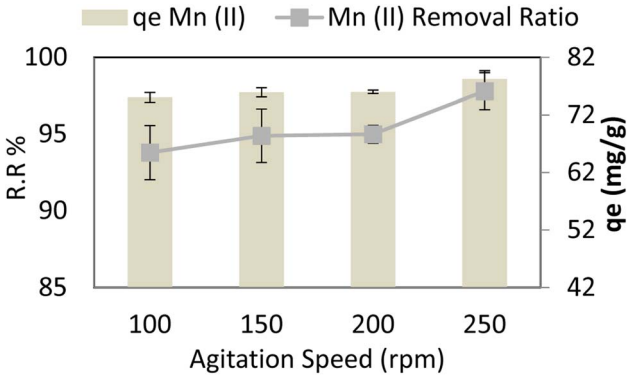

Fig. 10 The agitation speed effect on the removal efficiency and the adsorption capacity of Mn(II).

declines, and the removal of ions declines by around 10% as temperature rises.

3.6. Agitation speed

Stirring varied from 100 rpm to 250 rpm at adsorbent dose = 0.05 g per 100 ml, pH = 6, time = 30 min, and Mn C_o = 40 mg L^{-1} at 30 °C, and it is noted that adsorption capacity (q_e) and removal ratio (RR %) of manganese (Mn) slightly increases as stirring increases nearly constant, maximum removal ratio % RR and adsorption capacity (q_e) reached 97.8 R^2 (r 0.916, p 0.084) and 78.24 R^2 (r 0.916, p 0.084) respectively at 250 rpm as shown in Fig. 10. Strong stirring, however, causes nanocomposite and pollutant kinetics to continue, increasing the likelihood of collision and reducing the time needed for contact, as illustrated in Fig. 10.

3.7. Initial concentration effect. For the initial concentration experiment, Mn ions varied from 5 to 400 ppm l at 0.05 g per 100 ml of adsorbent, pH = 6, contact time = 30 min, and agitation speed = 250 rpm at 30 °C. It is observed that adsorption capacity (q_e) R^2 (r 0.455, p 0.257) and removal ratio (RR %) R^2 (r 1.00, p 0.00) of manganese Mn(II) increased at high concentration of (Mn) ions and decreased at low concentration of (Mn) ions, as shown in Fig. 11.

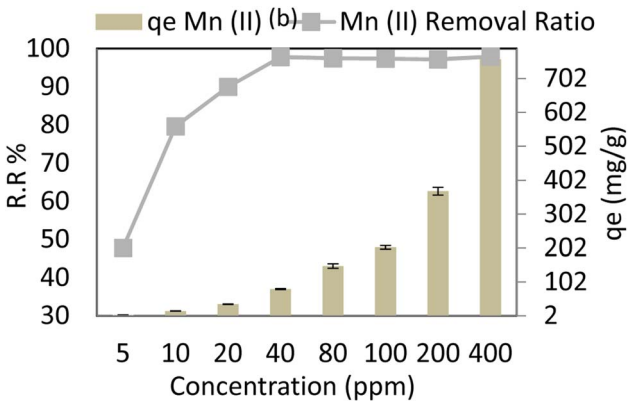

Fig. 11 Effect of concentration on the removal efficiency and the adsorption capacity of Mn(II).

With a constant amount of adsorbent, a higher initial manganese concentration causes a higher level of manganese in the solution, which increases the adsorbent's capacity to bind manganese. Due to a significant mass transfer forcing, the adsorption increases as manganese levels rise. Table 4 compares AgNP/GO/Chitosan nanocomposite removal efficiency and other materials for manganese Mn(II). It can be deduced from Table 4 that AgNP/GO/Chitosan nanocomposite possesses the highest removal efficiency and adsorption capacity.

3.8. Isothermal model

When evaluating the adsorption capacity of AgNP/GO/Chitosan and Mn(II) balancing features, four isotherm models—Langmuir, Freundlich, Dubinin–Radushkevich, and Tempkin—were utilized.[13]

3.8.1. Langmuir isotherm. According to data shown in Table 5, the coefficients of determination (R^2) for Mn(II) were (0.027 for linear and 0.884 for nonlinear). This indicates that the Mn(II) adsorption on AgNPs/Go/Chitosan is best suited with a nonlinear Langmuir isotherm. The linear, however, does not fit this description. For Mn(II), the q_o (mg g^{-1}) values were approximately (77.433 for linear and 643 985.5 for nonlinear) and K_L (0.089.79 for linear and 0.0001 for nonlinear). The material efficiency is shown by q_m, corresponding to the manganese Mn(II) for AgNPs/GO/Chitosan. Langmuir's isotherm covered that Mn(II) adsorption took place at functional groups or binding sites rather than monolayer adsorption on the adsorbent surface. One molecule thick, implying that the adsorption layer is only one molecule thick. The Langmuir model was not particularly well followed by AgNPs, GO, or chitosan. A dimensionless separation factor (R_L) can be used to determine the basic properties of the Langmuir isotherm as:

$$R_L = \frac{1}{1 + K_L C_o} \quad (3)$$

Using the Langmuir model study for Mn(II) adsorption on AgNPs/GO/Chitosan isotherm at room temperature, values for the K_L and q_m coefficients reported in Table 5 for this study can be calculated (25 °C).

The Langmuir model assumes only one solute molecule per site and a fixed number of sites. The Langmuir isotherm relates q_e (mg of adsorbate adsorbed per gram of adsorbent media) and C_e (the equilibrium adsorbate concentration in solution). As demonstrated in eqn (3), the Langmuir isotherm connects q_e (the amount of adsorbate adsorbed per gram of adsorbent media) and C_e (the equilibrium concentration of adsorbate in solution). Langmuir's constant, K_L, is represented in L mg^{-1}. The parameters of the adsorbent affect the maximum adsorption capacity; K_L (L mg^{-1}) is the Langmuir adsorption affinity constant connected to the bond energy of adsorption. The dimensionless separation factor constant (R_L), which offers important details on the nature of adsorption, can also be estimated using the Langmuir model. Adsorption is considered unfavourable when R_L is more than 1 and irreversible when R_L is

Table 4 Compares AgNP/GO/Chitosan nanocomposite removal efficiency and other materials for manganese Mn(II)

Adsorbent/method	Operating conditions	Capacity	Removal ratio of Mn(II)	Type of treated water	Ref.
Material of thermal power plants	pH 5.00 ppm Conc. 8.00 Temp 25 °C	—	47.2%	Aqueous solutions and wastewaters	35
Coal fly ash	pH 0.151 ppm Conc. 8.00 Temp 25 °C Stirrer 150 rpm Time 180 min Dose 0.2 g per 100 ml	—	27%	Aqueous solutions	36
Hydroxide precipitation	pH 8 Conc. 1791 ppm	—	71.4%	Synthetic laterite waste solution	37
Carbonate precipitation	pH 8 Conc. 1764 ppm	—	90.7%	Synthetic laterite waste solution	38
Sulfide precipitation	pH 7 Conc. 32.8 ppm	—	75%	Synthetic laterite waste solution	38
Coagulation/flocculation	pH 9.2	—	82%	Synthetic manganese sulfate solution	38
Oxidation/filtration	pH 8	—	30.6%	Synthetic groundwater $KMnO_4$ oxidation	38
Carbon impregnated with cetyl trimethyl ammonium bromide (CTAB)	pH 7 Conc. 50 ppm Temp 70 °C Time 420 min	43 mg g^{-1}	82.2%	Wastewater	38
Carbon impregnated with sodium dodecyl sulfate	pH 7 Conc. 50 ppm Temp 70 °C Time 420 min	47 mg g^{-1}	70.5%	Wastewater	38
Unmodified mesoporous carbon	pH 7 Conc. 50 ppm Temp 70 °C Time 420 min	40 mg g^{-1}	56.8%	Wastewater	38
Granular activated carbon	pH 7 Temp 25 °C Time 6 h	2.5451 mg g^{-1}	—	Wastewater	38
Granular activated carbon	pH 7 Temp 25 °C Time 30 min	79.05%, 2 mg g^{-1}	—	Wastewater	38
Chitosan/polyethylene glycol blend membrane	pH 3–6 Conc. 2–10 Temp 27 °C Stirrer 300 rpm Time 60 min	18 mg g^{-1}	—	Wastewater	38
Electrochemical treatment solutions	pH 7 Conc. 100 ppm	—	87.9%	Aqueous	38
AgNPs/GO/chitosan nanocomposite solutions and wastewaters	pH 6 Conc. 40 ppm Temp 30 °C Stirrer 250 rpm Time 30 min Dose 0.05 mg g^{-1}	1605 mg g^{-1}	97.9%	Aqueous	This study

Table 5 Langmuir isotherm models

Heavy metals	Langmuir model	Plotting	q_o (mg g^{-1})	K_L (L mg^{-1})	R_L	R^2
Mn(II)	Nonlinear : $q_e = q_o \frac{K_L C_e}{1 + K_L C_e}$ (1)	q_e *vs.* C_e	643 985.5	0.0001	0.982	0.884
	Linear: $C_e/q_e = 1/q_o K_L + C_e/q_o$ (2)	C_e/q_e *vs.* C_e	77.4333	0.089	0.690	0.027

Table 6 Freundlich isotherm models

Heavy metals	Freundlich model	Plotting	K_f ((mg g^{-1})/(mg L^{-1})^n)	n	R^2
Mn(II)	Nonlinear: $q_e = K_f C_e^{1/n}$ (3)	q_e *vs.* C_e	21.07036	0.594	0.999
	Linear : $\ln q_e = \ln K_F + \frac{1}{n} \ln C_e$ (4)	$\ln q_e$ *vs.* $\ln C_e$	23.94211	0.791	0.998

lower than 1. The adsorption is thought to be linear when R_L equals 1. The R_L values in Table 5 demonstrate that the circumstances were favourable for Mn(II) adsorption. The poor coefficients of determination ($R^2 = 0.88$) of AgNPs/GO/Chitosan provided further evidence that the Langmuir model for Mn(II) was unfavourable.

3.8.2. Freundlich isotherm. As $1/n$ approaches zero, an adsorption surface becomes more heterogeneous. The R^2 values in Table 6 make it obvious that the linear Freundlich model can account for the correlation between the concentration of Mn(II) adsorbing in biomass and its equilibrium concentration in solution. These numbers are, in turn, 0.998 for linear and 0.999 for nonlinear. The K_F and n values for AgNPs/GO/Chitosan were, respectively, (23.94211 for linear and 21.07036 for nonlinear mg g^{-1}) and (0.791 for linear and 0.594 for nonlinear) L^{-1} g, respectively. Mn(II) had an R^2 value of 0.999 in the nonlinear Freundlich model shown in Table 6. The nonlinear model could account for the adsorbed Mn(II) on AgNPs/GO/Chitosan at an equilibrium concentration in the solution.

The effectiveness of adsorbents in removing Mn(II) from the environment depends on various factors. Mn(II) was successfully adsorbed by AgNPs/GO/Chitosan biomass when the $1/n$ was between 0.00 and 1.00. When $1/n$ is less than 1, the surface functional area distribution or other factors may be to blame for reducing the adsorbent–adsorbate interaction. The Freundlich model asserts that saturation is not feasible since adsorption might occur on several levels. In equation, we can observe the Freundlich constant, n, and an adsorption capacity index, K_F (index of adsorption intensity or surface heterogeneity). K_F is based on the amount of Mn(II), which can be eliminated because their concentration levels are constrained using the adsorbent dosage. Tables 5–8 present the Mn(II) adsorption isotherms by the Langmuir, Freundlich, Dubinin–Radushkevich, and Tempkin isotherms, along with correlation values (R^2).

There are three isotherm models for Mn(II): the Freundlich isotherm (R^2 for nonlinear 0.999 for linear model 0.998), the Tempkin (R^2 for nonlinear 0.675 and linear 0.675), and the Dubinin–Radushkevich (R^2 for nonlinear 0.882 and linear 0.227). These indicate that while linear Dubinin–Radushkevich, linear Langmuir, and both Tempkin isotherm models cannot match the experimental data satisfactorily, nonlinear Freundlich, Dubinin–Radushkevich, and Langmuir isotherm models can.

The nonlinear and linear Freundlich modelling for the adsorption system fits the experimental data. The maximum adsorption capacity for Mn(II) determined by the nonlinear Dubinin–Radushkevich model was 932.25 mg g^{-1}, as shown in Table 7. Since the actual values for the adsorption system's saturation capacity are greater than those predicted by these models, the Dubinin–Radushkevich,[1] Langmuir, and Tempkin isotherm models are not applicable.

3.9. Models of kinetics

Pseudo-first-order and pseudo-second-order models were used to analyze the adsorption kinetics.[1]

3.9.1. The pseudo-first-order. The q_e value of the pseudo-first order model agreed with the estimated value, as shown in Table 9. Additionally, the correlation between the pseudo-first order model and Mn(II) was achieved ($R^2 = 0.141$ for linear and $R^2 = 0.199$ for nonlinear). Since the adsorption kinetics for Mn(II). Are linear and nonlinear, the pseudo-first-order model did not fit these data.

3.9.2. The pseudo-second-order. The q_e value derived by the pseudo-first order model agreed with the experimental results, as shown in Table 10. Additionally, for Mn(II), a correlation with the pseudo-second-order model was achieved ($R^2 = 0.980$ for linear and $R^2 = 0.927$ for nonlinear). As a result, Mn (IIadsorption)'s kinetics were linearly predicted by the pseudo-

Table 7 Dubinin–Radushkevich isotherm models

Heavy metals	Dubinin–Radushkevich model	Plotting	q_m	β	E (kJ mol^{-1})	R^2
Mn(II)	Nonlinear: $q_e = q_m \exp^{-\beta\varepsilon^2}$ (5)	q_e *vs.* ε^2	932.254	0.001	362.770	0.882
	Linear: $\ln q_e = \ln q_m - \beta\varepsilon^2$ (6)	$\ln q_e$ *vs.* ε^2	111.548	0.001	1282.79	0.227

Table 8 Tempkin models

Heavy metals	Tempkin model	Plotting	b	K_T	B	R^2
Mn(II)	Nonlinear : $q_e = \frac{RT}{b} \ln(K_T C_e)$ (7)	q_e *vs.* C_e	8.284	0.739	304.222	0.675
	Linear : $q_e = \frac{RT}{b} \ln K_T + \frac{RT}{b} \ln C_e$ (8)	q_e *vs.* $\ln C_e$	8.284	0.739	304.222	0.675

Table 9 The pseudo-first-order models

Heavy metals	The pseudo-first-order model	Plotting	k_1 (min^{-1})	q_e (mg g^{-1})	R^2
Mn(II)	Nonlinear: $q_t = q_e(1 - e^{-k_1 t})$ (1)	q_t *vs.* t	0.514	78.139	0.199
	Linear: $\log(q_e - q_t) = \log(q_e) - k_1 t/\ln 10$ (2)	$\log(q_e - q_t)$ *vs.* t	−0.020	0.099	0.141

Table 10 The pseudo-second-order model

Heavy metals	The pseudo-second-order model	Plotting	K_2 (g mg^{-1} min^{-1})	q_e (mg g^{-1})	R^2
Mn(II)	Nonlinear: $q_t = k_2 {q_e}^2 t/(1 + k_2 q_e t)$ (3)	q_t *vs.* t	0.199	78.140	0.017
	Linear: $t/q_t = 1/(k_2 {q_e}^2) + t/q_e$ (4)	t/q_t *vs.* t	−0.0006	92.514	0.940

second-order model, but Mn (Mnadsorption)'s kinetics were nonlinear (II). The experimental q_e mg g^{-1} for Mn(II) and the calculated q_e (78.140 nonlinear, 92.514 linear) mg g^{-1}, respectively, are calculated using the pseudo-second-order model and are shown in Table 10. The cations of the pollutants attach to the adsorbent surfaces *via* chemical interactions (typically covalent bonds). In the pseudo-second-order chemisorption model, they seek regions where their coordination number with the surface is highest.

3.10. Diffusion model

Weber and Morris evaluated the intraparticle diffusion hypotheses. The adsorbate's diffusion determines the adsorption rate toward the adsorbent in the intraparticle dissemination display (*i.e.*, the process is dispersion controlled). Adsorption morphologies are presented.[13]

The results of this investigation show that depending on the initial Mn(II) load, different amounts of Mn(II) are adsorbed. Four processes are assumed to be involved in the removal of Mn(II) by adsorption: bulk diffusion, (ii) film diffusion, (ii) pore or intra-particle diffusion, and (iv) pollutant adsorption on the surface of the sorbent. The literature suggests that if the stirring speed is sufficiently high, the first step may be "ignored," as was previously mentioned. An intraparticle diffusion plot shows a boundary layer effect early in the adsorption process. The second portion of the linear curve represents the progressive adsorption stage, during which intraparticle diffusion has changed into a charge-limiting process. A third part, the equilibrium stage, is created when adsorbate concentrations fall and intraparticle diffusion begins to slow. K_{id} and C were calculated using the second linear segment. The intraparticle diffusion parameters for the adsorption process are determined and shown in the Tables below Tables 11–13. Although it did not proceed *via* the origin, there was a straight relationship between the times. It suggested that because intraparticle was obvious, it was not the only rate-controlling stage and that there might be other mechanisms at play.[33]

As shown in Tables 11–13, the AgNPs/GO/Chitosan adsorbents deviate from the linear parts of the plots at the origin of

Table 11 Intraparticle diffusion models

Heavy metals	Intraparticle diffusion model	Plotting	k_1 (mg g^{-1} min$^{-0.5}$)	C (mg g^{-1})	R^2
Mn(II)	Nonlinear: $q = k_i t^{0.5} + C$ (5)	q *vs.* t	−0.047	78.048	0.061
	Linear: $q = k_i t^{0.5} + C$ (5)	q *vs.* $t^{0.5}$	−0.047	78.333	0.061

Table 12 Pore diffusion models

Heavy metals	Pore diffusion model	Plotting	k_p (min$^{-0.5}$)	D_{ii} (cm^2 min^{-1})	R^2
Mn(II)	$\frac{q_t}{q_e} = F = \frac{6}{r_o}\left(-\frac{D_{ii} t}{\pi}\right)^{1/2} = k_p \times t^{1/2}$ (6)	$\frac{q_t}{q_e}$ *vs.* $t^{0.5}$	0.148	0.00001	0.061

Table 13 Film diffusion models

Heavy metals	Film diffusion model	Plotting	k_{fd} (min^{-1})	D_{ii} (cm^2 min^{-1})	R^2
Mn(II)	$\ln\left(1 - \frac{q_t}{q_e}\right) = -\left(\frac{D_i}{{r_o}^2}\right)\pi^2 t = -k_{fd} t$ (7)	$\ln\left(1 - \frac{q_t}{q_e}\right)$ *vs.* t	0.096	0.0001	0.141

the q_t *vs.* $t^{1/2}$ plots. As a result, the Mn(II) adsorption on AgNPs/GO/Chitosan is complicated, and the adsorption process is still not entirely monitored by the intra-particle diffusion stage of AgNPs/GO/Chitosan adsorption.[33] Plotting Mn(II) uptake (q_t/q_e) *vs.* $t^{0.5}$ reveals portions that correspond to a highly rapid beginning stage followed by a gradual final uptake of the ions into the pores, which was consistent with the trend found in the Weber and Morris intra-particle diffusion model. Researchers suggested examining the adsorption process utilizing film diffusion and pore diffusion to understand more about the processes and rate-controlling phases affecting adsorption kinetics. The film diffusion equation can be expressed as:

$$\frac{q_t}{q_e} = 6\left(\frac{D_1}{\pi a^2}\right)^{0.5} t^{0.5} + C \quad (4)$$

A (μm) is the average AgNPs/Go/Chitosan radius, and D_1 is the film diffusion coefficient ($\mu m^2\ S^{-1}$).

The exterior of the AgNPs/GO/Chitosan nanocomposite affects the boundary layer Mn(II) ion transport. The three portions of intraparticle diffusion are consistent with the plot of q_t/q_e against $t^{0.5}$ for Mn(II) uptake. It can be easier to comprehend the pore diffusion model if you compare it to the adsorption kinetics. According to Reichenberg's formulation of the pore diffusion equation:

$$\frac{q_t}{q_e} > 0.85,\ B_t = -0.4977 - \ln\left(1 - \frac{q_t}{q_e}\right) \quad (5)$$

$$\frac{q_t}{q_e} < 0.85,\ B_t = \left(\sqrt{\pi} - \sqrt{\pi - \left(\frac{\pi^2}{3} \times \frac{q_t}{q_e}\right)}\right)^2 \quad (6)$$

Mn(II) fractional uptake (q_t/q_e) as a function of time, $t^{0.5}$, squared. Plots of Mn(II) fractional absorption *vs.* time ($t^{0.5}$) for AgNPs, GO, and Chitosan, respectively. Similar to the trend found in the intraparticle diffusion plot, it was discovered that the plots had sections that represented a very rapid early stage followed by a gradual final uptake of Mn(II) ions into the pores. Tables demonstrate the film diffusion coefficient (D_1) values for Mn(II) adsorption onto AgNPs/GO/Chitosan based on the slope of the q_t/q_e against $t^{0.5}$ graphs Tables 9–11. AgNPs/GO/higher Chitosan's D_1 values may be explained by two factors: the positively charged Mn(II), which is produced in a higher percentage for this system, experiences repulsion as it travels through the liquid film to the positively charged adsorbent surface at pH, and the roughness the adsorbent has caused to the surface. It was found that[34] had a film diffusion coefficient between 10^{-6} and 10^{-8} $cm^2\ s^{-1}$, proving that the adsorption mechanism uses film diffusion. Our study's measurement of the film diffusion coefficient for AgNPs/GO/Chitosan was 10^{-7}, suggesting that film diffusion may have played a role in the Mn(II) adsorption onto AgNPs/GO/Chitosan.

We can use B for the effective pore diffusion coefficient, D_2 ($\mu m^2\ S^{-1}$), from the following equation

$$B = \pi \frac{D_2}{r^2} \quad (7)$$

Under the ideal conditions of linearity, pore-diffusion control can fully explain the mass transfer rate (B_t *vs.* t plot). If the graph is nonlinear or linear with a nonzero intercept, film diffusion or a chemical reaction will affect the adsorption rate. The graphs of B_t *vs.* t for Mn(II) suggest that either film-diffusion or chemical reaction was the driving force behind the adsorption process because nonlinear sections first showed in the plot of B_t/t for Mn(II) at low adsorption durations.

3.11. Column adsorption

Glass columns with an inner diameter of 4.0 cm were used to study continuous flow adsorption. All column experiment procedures have been done, as in El Shahawy *et al.* (2022).[30] The saturation capacity of adsorbent composites of AgNPs, GO, and chitosan was evaluated in columns using the equation:

$$q_e = \int_0^{ve} (C_o - C)dv/m \quad (8)$$

where q_e represents the Mn adsorbed ($mg\ g^{-1}$), the concentration of Mn in feed water is C_o (ppm), and C is the outlet Mn concentration (ppm). The solvent volume needed to achieve the point of exhaustion is known as ve (L), and m is the mass of the adsorbent (g).

3.11.1. Effect of flow rate. The adsorption columns were run at 3, 6, and 10 ml min^{-1} flow rates until no more Mn could be extracted. The breakthrough curve for a column was produced by plotting the C_e/C_o ratio with time (where C_e and C_o stand for the Mn concentrations in treated wastewater and feed water, respectively). This breakthrough curve is shown in Fig. 12. The column operated excellently at the lowest flow rate of 3 ml min^{-1}. By increasing the flow rate from 3 to 10 ml min^{-1}, the manganese breakthrough and extraction periods were shortened, and the Mn column breakthrough time was decreased from 80 to 60 minutes. Less Mn was absorbed because the residence period was shortened, reducing Mn(II) interaction with the adsorbent AgNP/GO/chitosan composites and fine sand. When flow rates were raised, the Mn ions left the column, preventing the adsorbent and fine sand column from reaching equilibrium.

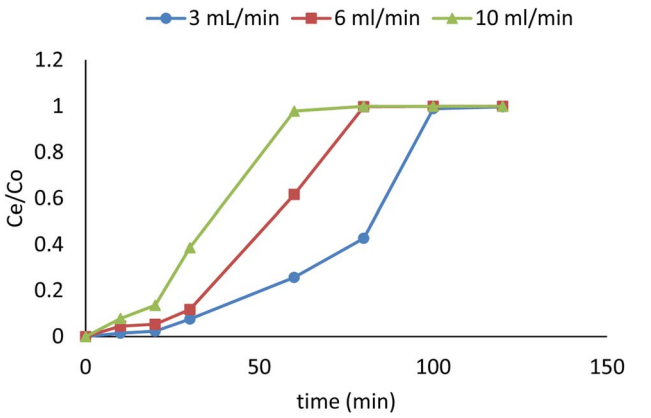

Fig. 12 Breakthrough curves expressed as C_e/C_0 *vs.* time.

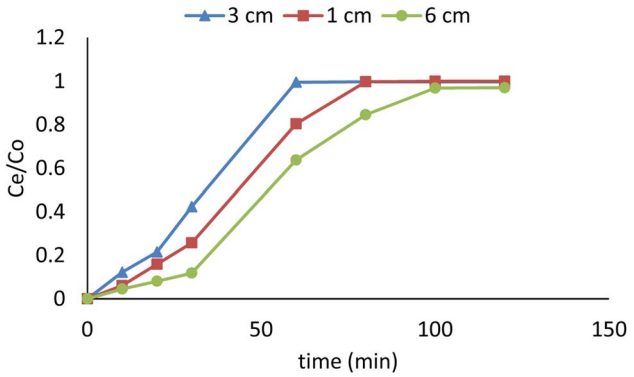

Fig. 13 Breakthrough curves expressed as C_e/C_0 *vs.* time.

3.11.2. Effect of bed height. The impact of AgNPs/GO/chitosan composite fine sand on Mn was examined using three different bed heights: 1 cm, 3 cm, and 6 cm. Mn solutions with a fixed concentration (49.29 ppm) were passed through a fixed-bed column at a constant flow rate of 6 ml min^{-1}. According to Fig. 13, the breakthrough time varied depending on bed height. Steeper breakthrough curves were produced as bed depth was reduced. Because there were fewer binding sites at shallower bed depths, the breakthrough time was reduced from 6 to 1 cm at bed depth. Mn ions do not have enough time to diffuse through the surface in composite adsorbents consisting of AgNPs, GO, and Chitosan with low bed depth, lowering breakthrough time. Due to the increased bed depth, the Mn ions could penetrate deeper into the AgNPs/GO/chitosan composite adsorbent and fine sand, extending the manganese solution's time inside the column.

4. Conclusion

The following conclusions can be drawn from the findings and discussions of the previous experiments:

(1) Heavy metal removal from wastewater effluent was optimized *via* adsorption.

(2) The (101) crystal plane at 55.1° has the largest XRD peak. AgNP/GO/Chitosan composites lacked 2 = 10.1° diffraction peaks, indicating that GO was reduced to rGO. As oxygen-containing energy groups disappear, van der Waals interactions reduce layer spacing. Improved thermal stability and electrical conductivity. AgNPs nanocrystals were tetragonal. All AgNP/GO composites had the same shape and particle sizes as AgNPs due to the same preparation circumstances. TEM and XRD particle readings were similar.

(3) The nanoparticles' external surface SEM allowed for structural observation. Chitin's surface morphology was surface with both bores and nanofibers, with an average particle size of 33.64 to 74.87 nm. The microfibril chitin fibers have a diameter of 1–2 μm and GO a thickness of 150 nm. There were no macro pores or defects in the final thin-layered membrane, as shown by the SEM image. The surface of graphite oxide sheets was visible, and the AgNPs were well dispersed and intertwined. This graphene oxide was visible on the surface of the sheets. There are no longitudinal incisions or bulges on the surface of AgNP/GO/Chitosan composite monolayers.

(4) GO's phenols, carbohydrates, and O–H form a 900 nm infrared peak. The absorption peak at 800 nm shows C=O bonds. The C–O–H bond peak is 1600 nm. CH bond causes a 3500 nm signal.

(5) Nonlinear and linear Freundlich models fit the experimental data with R^2 values of 0.999 and 0.998, respectively.

(6) The pseudo-second-order linear model was a good fit for the experimental data, with an R^2 of 0.940 for eliminating Mn(II) using AgNP/GO/Chitosan.

(7) The pore diffusion model predicted an excellent agreement with actual data for Mn(II) and AgNP/GO/Chitosan removal ($R^2 = 0.061$).

(8) A thermodynamic model revealed the approach is viable, and the negative G value confirmed Mn(II) adsorption on AgNP/GO/Chitosan is spontaneous. The process is exothermal because G decreases with temperature. Temperature increases decreased Mn removal (II). Positive H suggests endothermic adsorption. S increases unpredictability at the solid–liquid interface during adsorption. Mn(II) adsorption on AgNP/GO/Chitosan was studied.

Abbreviations

FTIR	Fourier transform infra-red
SEM	Scanning electron microscopic
TEM	Transpiration electro microscopic
COD	Chemical oxygen demand
TDS	Total dissolved solids
XRD	X-ray diffraction
TSS	Total suspended solids
AlK	Alkalinity

List of materials

W.W	Industrial wastewater
Cs	Chitosan
Ct	Chitin
HCl	Hydrochloric acid
NaOH	Sodium hydroxide
GO	Graphite powder
$AgNO_3$	Silver nitrate
$NaBH_4$	Sodium borohydride
$C_6H_5Na_3O_7 \cdot 2H_2O$	Trisodium citrate dihydrate
$MnCl_2$	Manganese chloride
AgNPs	Silver nanoparticles
$CaCO_3$	Calcium carbonate
$CaCL_2$	Calcium chloride
CO	Carbon dioxide
Dw	Distilled water

Conflicts of interest

There are no conflicts to declare.

Acknowledgements

The authors thank Suez Canal University's Centre for Environmental Studies and Consultants in Ismailia, Egypt.

References

1 A. Pholosi, E. B. Naidoo and A. E. Ofomaja, Intraparticle diffusion of Cr(VI) through biomass and magnetite coated biomass: A comparative kinetic and diffusion study, *S. Afr. J. Chem. Eng.*, 2020, **32**, 39–55, DOI: 10.1016/j.sajce.2020.01.005.

2 A. Abass, *Complete International Law*, Oxford University Press, 2012, ISBN:9780199578702.

3 Y. A. E. H. Ali, A. D. N'diaye, D. Fahmi, M. S. A. Kankou and M. Stitou, Adsorption of Congo red from aqueous solution using Typha australis leaves as a low cost adsorbent, *J. Environ. Treat. Tech.*, 2021, **9**(2), 534–539.

4 Y. Sanou and S. Pare, Comparative Study of Adsorption Capacity of Two Mixed Materials for Arsenic Remediation, *J. Environ. Treat. Tech.*, 2021, **9**(3), 559–565.

5 I. N. C. E. Muharrem and O. K. Ince, An overview of adsorption technique for heavy metal removal from water/wastewater: a critical review, *Int. J. Pure Appl. Sci. Technol.*, 2017, **3**(2), 10–19.

6 K. Pakshirajan and T. Swaminathan, Biosorption of Copper and Cadmium in Packed Bed Columns with Live Immobilized Fungal Biomass of Phanerochaete chrysosporium, *Appl. Biochem. Biotechnol.*, 2009, **157**(2), 159–173, DOI: 10.1007/s12010-008-8283-3.

7 S. S. Raheem, M. A. Al-Dossary and H. T. AL-Saad, Determination of Carbendazim Fungicide and Oxymatrine Insecticide Residues in the Soils of Four Agriculture Stations in Basrah Governorate by HPLC, *J. Biol. Agric. Healthcare*, 2017, **7**, 10–16.

8 S. Omar, M. S. Muhamad, L. Te Chuan, T. Hadibarata and Z. C. Teh, A Review on Lead Sources, Occurrences, Health Effects, and Treatment Using Hydroxyapatite (HAp) Adsorbent Made from Fish Waste, *Water, Air, Soil Pollut.*, 2019, **230**(12), 1–21, DOI: 10.1007/s11270-019-4312-9.

9 A. Samanta, S. Das and S. Jana, Exploring $β$-FeOOH Nanorods as an Efficient Adsorbent for Arsenic and Organic Dyes, *ChemistrySelect*, 2018, **3**(9), 2467–2473, DOI: 10.1002/slct.201703022.

10 N. Marsidi, H. Abu Hasan and S. R. Sheikh Abdullah, A review of biological aerated filters for iron and manganese ions removal in water treatment, *J. Water Process. Eng.*, 2018, **23**(October 2017), 1–12, DOI: 10.1016/j.jwpe.2018.01.010.

11 A. P. Devi, D. K. Padhi, P. M. Mishra and A. K. Behera, Bio-Surfactant assisted room temperature synthesis of cubic Ag/RGO nanocomposite for enhanced photoreduction of Cr (VI) and antibacterial activity, *J. Environ. Chem. Eng.*, 2021, **9**(2), 104778, DOI: 10.1016/j.jece.2020.104778.

12 Y. Fei and Y. H. Hu, Design, synthesis, and performance of adsorbents for heavy metal removal from wastewater: a review, *J. Mater. Chem. A*, 2022, **10**(3), 1047–1085, DOI: 10.1039/d1ta06612a.

13 A. S. Eltaweil, H. Ali Mohamed, E. M. Abd El-Monaem and G. M. El-Subruiti, Mesoporous magnetic biochar composite for enhanced adsorption of malachite green dye: Characterization, adsorption kinetics, thermodynamics and isotherms, *Adv. Powder Technol.*, 2020, **31**(3), 1253–1263, DOI: 10.1016/j.apt.2020.01.005.

14 K. Jiang, D. P. Lepak and J. C. Baer, How does human resource management influence organizational outcomes? A meta-analytic investigation of mediating mechanisms Kaifeng Jiang, *Acad. Manag. J.*, 2012, **55**(6), 1264–1294.

15 I. Mohmood, C. B. Lopes and I. Lopes, Nanoscale materials and their use in water contaminants removal—a review, *Environ. Sci. Pollut. Res.*, 2013, **20**(3), 1239–1260, DOI: 10.1007/s11356-012-1415-x.

16 C. Ragasa, A. Dankyi, P. Acheampong, A. N. Wiredu and A. Chapo, *Patterns of Adoption of Improved Rice Technologies in Ghana*, 2013.

17 T. L. Gerke, B. J. Little and J. Barry Maynard, Manganese deposition in drinking water distribution systems, *Sci. Total Environ.*, 2016, **541**, 184–193, DOI: 10.1016/j.scitotenv.2015.09.054.

18 H. Du, A nonlinear filtering algorithm for denoising HR(S)TEM micrographs, *Ultramicroscopy*, 2015, **151**, 62–67, DOI: 10.1016/j.ultramic.2014.11.012.

19 F. Boudrahem, F. Aissani-Benissad and A. Soualah, Removal of basic yellow dye from aqueous solutions by sorption onto reed as an adsorbent, *Desalin. Water Treat.*, 2015, **54**(6), 1727–1734, DOI: 10.1080/19443994.2014.888686.

20 J. H. Kim, J. A. Park, J. K. Kang, *et al.*, Phosphate sorption to quintinite in aqueous solutions: Kinetic, thermodynamic and equilibrium analyses, *Desalin. Water Treat.*, 2015, **20**(1), 73–78, DOI: 10.4491/eer.2014.053.

21 X. Sun, L. Yang, H. Xing, *et al.*, High capacity adsorption of Cr(VI) from aqueous solution using polyethylenimine-functionalized poly(glycidyl methacrylate) microspheres, *Colloids Surf., A*, 2014, **457**(1), 160–168, DOI: 10.1016/j.colsurfa.2014.05.061.

22 Z. Wang, Y. Li, D. Kong, *et al.* Acquisition of Epithelial-Mesenchymal Transition Phenotype of Gemcitabine-Resistant Pancreatic Cancer Cells Is Linked with Activation of the Notch Signaling Pathway, *Cancer Res.*, 2009, **69**(6), 2400–2408, DOI: 10.1158/0008-5472.CAN-08-4312.

23 D. Radosavljević, The Alchemy of Power and Freedom–A Contextualisation of Slobodan Šnajder's Hrvatski Faust (The Croatian Faust), *Contemp. Theatre Rev.*, 2009, **19**(4), 428–447.

24 D. Radosavljević, The Alchemy of Power and Freedom–A Contextualisation of Slobodan Šnajder's Hrvatski Faust (The Croatian Faust), *Contemp. Theatre Rev.*, 2009, **19**(4), 428–447.

25 S. D. Crausbay, A. R. Ramirez and S. L. Carter, Defining Ecological Drought for the Twenty-First Century, *Bull. Am. Meteorol. Soc.*, 2017, **98**(12), 2543–2550, DOI: **10.1175/BAMS-D-16-0292.1**.

26 M. Wan, Z. Liu, S. Li, *et al.*, Silver nanoaggregates on chitosan functionalized graphene oxide for high-performance surface-enhanced Raman scattering, *Appl. Spectrosc.*, 2013, **67**(7), 761–766, DOI: **10.1366/12-06777**.

27 Y. Feng, L. Yang, J. Liu and B. E. Logan, Electrochemical technologies for wastewater treatment and resource reclamation, *Environ. Sci.: Water Res. Technol.*, 2016, **2**(5), 800–831, DOI: **10.1039/c5ew00289c**.

28 P. T. Thi, T. Van Khai, T. X. Diem, C. N. T. Nghia, T. T. T. Ngan, N. N. Vinh and N. M. Hien, Synthesis of Ag/GO nanocomposite with promising photocatalytic ability for reduction reaction of p-nitrophenol, *Mater. Res. Express*, 2021, **8**(10), 105009.

29 A. El Shahawy, M. F. Mubarak, M. El Shafie and H. M. Abdulla, Fe(III) and Cr(VI) ions' removal using AgNPs/GO/chitosan nanocomposite as an adsorbent for wastewater treatment, *RSC Adv.*, 2022, **12**(27), 17065–17084.

30 A. El Shahawy, M. F. Mubarak, M. El Shafie and H. M. Abdulla, Fe(iii) and Cr(vi) ions removal using AgNPs/GO/chitosan nanocomposite as an adsorbent for wastewater treatment, *RSC Adv.*, 2022, **12**(27), 17065–17084, DOI: **10.1039/d2ra01612e**.

31 N. Arshad and S. Imran, Indigenous waste plant materials: An easy and cost-effective approach for the removal of heavy metals from water, *Curr. Res. Green Sustainable Chem.*, 2020, **3**, 100040, DOI: **10.1016/j.crgsc.2020.100040**.

32 J. Trujillo-Reyes, J. R. Peralta-Videa and J. L. Gardea-Torresdey, Supported and unsupported nanomaterials for water and soil remediation: Are they a useful solution for worldwide pollution?, *J. Hazard. Mater.*, 2014, **280**, 487–503, DOI: **10.1016/j.jhazmat.2014.08.029**.

33 A. S. Eltaweil, E. M. Abd El-Monaem, H. M. Elshishini, et al., Recent developments in alginate-based adsorbents for removing phosphate ions from wastewater: a review, *RSC Adv.*, 2022, **12**(13), 8228–8248, DOI: **10.1039/d1ra09193j**.

34 P. Chen, J. Bornhorst and M. Aschner, Manganese metabolism in humans, *Front. Biosci.-Landmark*, 2018, **23**(9), 1655–1679, DOI: **10.2741/4665**.

35 N. Sharma, S. K. Maiti and K. K. Sharma, Prevalence, etiology and antibiogram of microorganisms associated with sub-clinical mastitis in Buffaloes in Durg, Chhattisgarh State (India), *Int. J. Dairy Sci.*, 2007, **2**(2), 145–151, DOI: **10.3923/ijds.2007.145.151**.

36 S. Mohan and R. Gandhimathi, Removal of heavy metal ions from municipal solid waste leachate using coal fly ash as an adsorbent, *J. Hazard. Mater.*, 2009, **169**(1–3), 351–359, DOI: **10.1016/j.jhazmat.2009.03.104**.

37 M. Nasrollahzadeh, M. Sajjadi, J. Dadashi and H. Ghafuri, Pd-based nanoparticles: Plant-assisted biosynthesis, characterization, mechanism, stability, catalytic and antimicrobial activities, *Adv. Colloid Interface Sci.*, 2020, **276**, 102103, DOI: **10.1016/j.cis.2020.102103**.

38 D. S. Patil, S. M. Chavan and J. U. K. Oubagaranadin, A review of technologies for manganese removal from wastewaters, *J. Environ. Chem. Eng.*, 2016, **4**(1), 468–487, DOI: **10.1016/j.jece.2015.11.028**.